Supporting information for

Chameleon-Inspired Strain-Accommodating Smart Skin

Yixiao Dong,[†] Alisina Bazrafshan,[†] Anastassia Pokutta,[‡] Fatiesa Sulejmani,[‡] Wei Sun,[‡] J. Dale Combs,[†] Kimberly C. Clarke,[†] and Khalid Salaita[*,†]

[†] Department of Chemistry, Emory University, Atlanta, Georgia 30322, United States.

[‡] Wallace H. Coulter Department of Biomedical Engineering, Georgia Institute of Technology, Atlanta, Georgia 30332, United States.

Table of Contents

Supplementary S1: Estimation of strain in conventional responsive photonic crystal gels

The diffraction of RPC gels can be estimated by the following equation,[1,2]

$$m\lambda = 2nd\sin\theta \qquad \text{(equation S1)}$$

where λ is the diffraction wavelength, d is the lattice spacing, θ is the angle of incidence, m is the diffraction order (considering the first order diffraction, m=1), n is the overall refractive index of the photonic crystal gels. According to previous studies,[3] n can be calculated as the average refractive index as below,

$$n_{avg} = \phi n_{particle} + (1 - \phi)n_{matrix} \qquad \text{(equation S2)}$$

where ϕ is the volume fraction of the particle in RPC gel, $n_{particle}$ is the refractive index of nanoparticles that form the photonic crystal structure. n_{matrix} is the refractive index of the hydrogel matrix (pNIPAM in this work). In our work, the content of nanoparticles in RPC gels is below 0.5 wt.%, and therefore, $n_{avg} \approx n_{matrix}$. Also, the change in refractive index[4] as a result of the phase transition of pNIPAM is less than 1wt%, thus we can treat the refractive index as a constant value here. We use n_0 to symbolize the refractive index of pNIPAM hydrogel. The final equation can be rewritten as,

$$\lambda = 2n_0 d\sin\theta \qquad \text{(equation S3)}$$

In this equation, the diffraction wavelength is proportional to the lattice distance.

1) If θ=90°, then $\sin\theta = 1$, $d = \lambda/2n_0$. For a sample with an original diffractive wavelength of 500 nm, and a blue shift of $\Delta\lambda$ = 100 nm, the overall change in d is as large as 20%. In other words, the strain in the sample is 20%.
2) If θ<90°, then $\sin\theta$<1, $d = \lambda/2n_0\sin\theta$ (d>$\lambda/2$). In the same case as of 1), the deswelling ratio must be larger than 20% strain. The results are 23.1% if θ=60° and 40% if θ=30°.

These calculations explain the inevitable large-scale swelling/deswelling behavior of traditional RPC gels. Note that this calculation represents a lower bound estimation of the required strain because we ignore the volume of the nanoparticles comprising the PC. Because the particles are incompressible, the actual required deswelling of the hydrogel must be longer than our current estimation.

Supplementary S2: Finite element analysis

A thermal stress model was applied for all the mechanical calculations used in this work.[5] First, thermal strains were calculated according to the equation below,

$$\varepsilon_{th} = \alpha(T)(T - T_{ref})$$

(equation S4)

Where ε_{th} is the strain of thermal expansion. $\alpha(T)$ is the coefficient of thermal expansion (linear). This coefficient was set as -0.01 to simulate the deswelling of pNIPAM. The temperature jump used for these calculations $(T - T_{ref})$ was set to 50 K, which justifies the assumed linear shrinkage of 50%.

Next, the solid mechanics were calculated based on the series of equations indicated below:

$$0 = \nabla \cdot \sigma$$

(equation S5)

$$\varepsilon_{el} = s : \sigma$$

(equation S6)

$$\varepsilon = \frac{1}{2}\left[(\nabla u)^{T} + \nabla u\right]$$

(equation S7)

$$\varepsilon = \varepsilon_{el} + \varepsilon_{th}$$

(equation S8)

The parameters used in equations 5-8 are detailed in **Table S1** below.

Table S1. Parameters used for solid mechanics calculations

| Parameter	Expression
Stress	$\sigma = \begin{pmatrix} \sigma_{xx} & \tau_{xy} & \tau_{xz} \\ \tau_{yx} & \sigma_{yy} & \tau_{yz} \\ \tau_{zx} & \tau_{zy} & \sigma_{zz} \end{pmatrix}$
Strain(total)	$\varepsilon = \begin{pmatrix} \varepsilon_{xx} & \gamma_{xy} & \gamma_{xz} \\ \gamma_{yx} & \varepsilon_{yy} & \gamma_{yz} \\ \gamma_{zx} & \gamma_{zy} & \varepsilon_{zz} \end{pmatrix}$
Thermal strain	$\varepsilon_{th} = \begin{pmatrix} \varepsilon_{xx}^{th} & \gamma_{xy}^{th} & \gamma_{xz}^{th} \\ \gamma_{yx}^{th} & \varepsilon_{yy}^{th} & \gamma_{yz}^{th} \\ \gamma_{zx}^{th} & \gamma_{zy}^{th} & \varepsilon_{zz}^{th} \end{pmatrix}$
Elastic strain	$\varepsilon_{el} = \begin{pmatrix} \varepsilon_{xx}^{el} & \gamma_{xy}^{el} & \gamma_{xz}^{el} \\ \gamma_{yx}^{el} & \varepsilon_{yy}^{el} & \gamma_{yz}^{el} \\ \gamma_{zx}^{el} & \gamma_{zy}^{el} & \varepsilon_{zz}^{el} \end{pmatrix}$
Elastic compliance coefficient	S (a fourth order tensor)
differential operator	$\nabla = \begin{pmatrix} \dfrac{\partial}{\partial x} \\ \dfrac{\partial}{\partial y} \\ \dfrac{\partial}{\partial z} \end{pmatrix}$
Displacement	$u = \begin{pmatrix} u_x \\ u_y \\ u_z \end{pmatrix}$
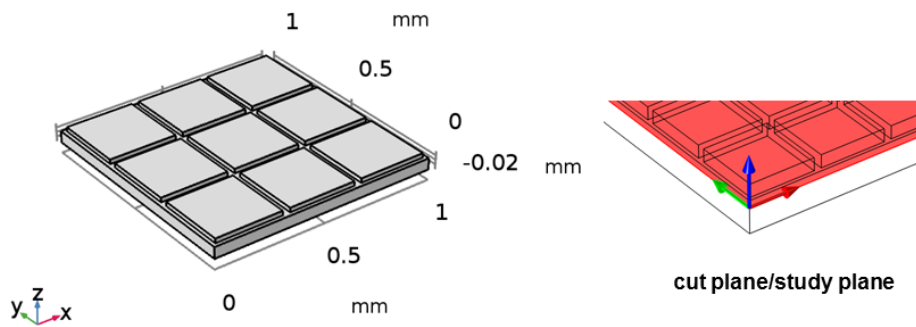
Figure S1. The model build for the finite element analysis calculations with a top-layer array of 3×3 (left) and the chosen cut plane for deformation and force calculations (right).

A typical model built for finite element analysis is show in **Figure S3**. The dimensions of the bottom layer were 1×1×0.05 mm. The number (*Num*) of top-layer squares in a row can vary from 1 to 9. To guarantee that the overall area of the top layer is constant, the side length of each square was defined as 0.9 mm/*Num*. Note that the dimensions of the model are smaller than those used for the experimental samples; however, we were focused on the relative trends as predicted by the computational analysis. Thus, the specific dimensions used in the calculations are not critical for our conclusions.
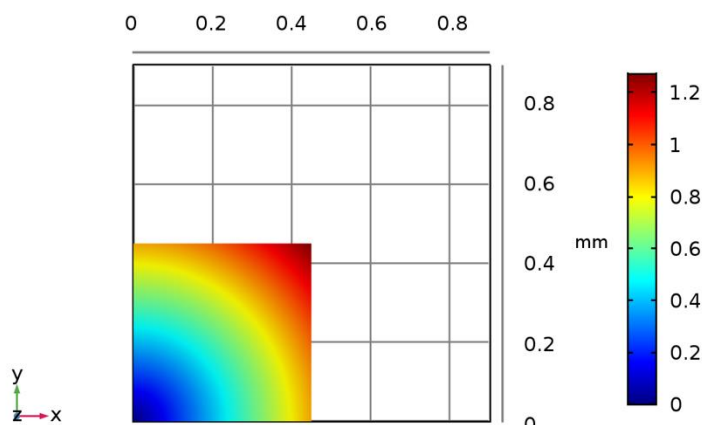
Figure S2. Plot of total displacement of a responsive (pNIPAM) film. For this calculation, we assumed a 50% linear shrinkage of the responsive layer that was suspended without a supporting polymer layer. One corner of the structure was fixed (x, y, z) = (0, 0, 0), and thus the structure shrank towards the fixed point. The colored heat map indicates the total displacement in units of mm.
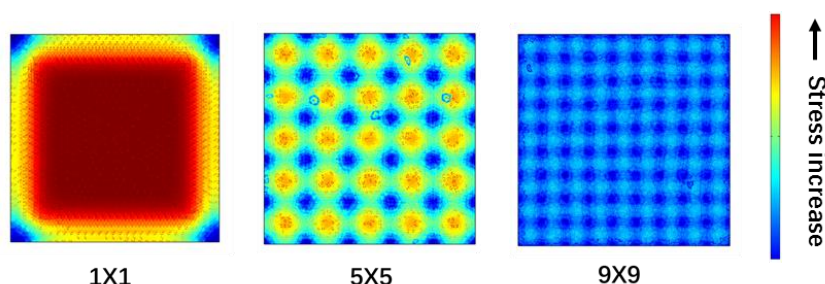

Figure S3. Images represent plots of von Mises stress for SASS structures that have been patterned with specific densities of square arrays. The Von mises stress values were obtained from a specific cut plane (see **Figure S2**).

von Mises stress analysis of a chosen cut plane further revealed a relationship between the number of tiles that a SASS material was divided to, and the Von mises stress (**Figure S4**). We found that fabricating SASS films with more finely patterned square arrays leads to a decrease in the accumulated strain. This observation can be partially explained because the patterned arrays spread the stress over a greater area as the structure is more finely patterned. In other words, the split structure provides more interstitial "space" between the responsive PC elements to dissipate and spread the accumulated stress.

We used one-dimensional strain analysis to further reveal the strain-accommodating behavior of SASS (**Figure S4**). The displacement field in **Figure S4(b)** shows staircase-shaped plots across distance (Arc length) of the red line depicted in **Figure S4(a)**. The plot

demonstrates that increasing the number of squares in a row (from 1x1 to 9x9), leads to more frequent "steps" across the same distance, which decreases the total displacement of the material. Each step corresponds to the space between the responsive polymer squares. In other words, the elastic deformation of the interstitial space dampens the total displacement so that the overall material is less deformed (**Figure S4 (b)** and **(c)**). Therefore, fabricating higher density square arrays (miniaturizing the patterns) in the responsive top layer increases the strain capacitance of the supporting material. These calculations provide a quantitative prediction of the strain-accommodating behavior for SASS.
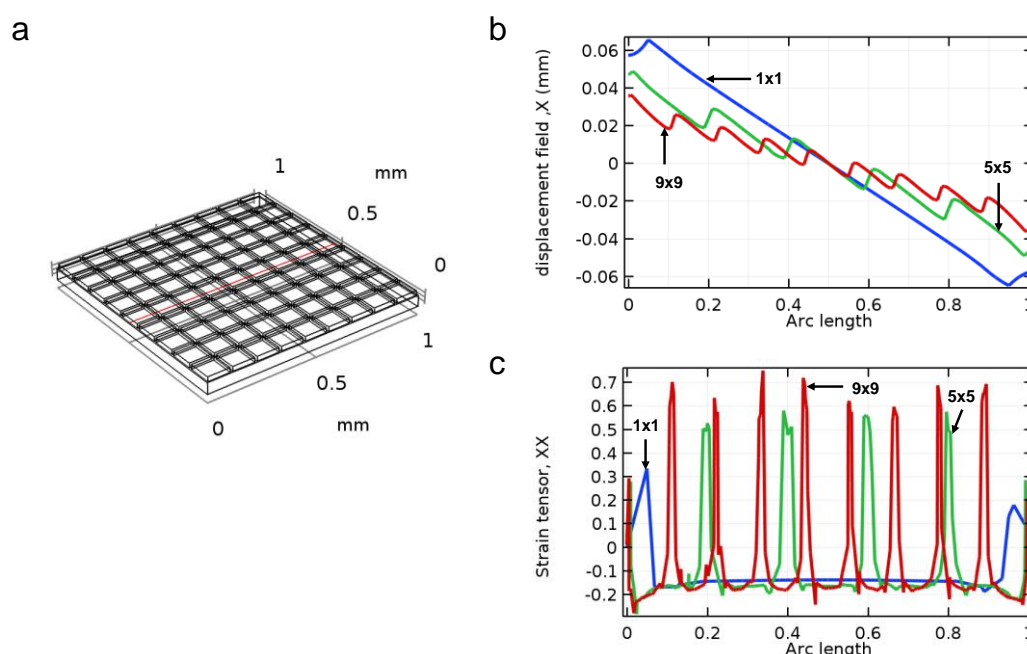

Figure S4. Computational prediction of strain values across the *x* direction of SASS films. **a.** 3D wire mesh rendering of SASS denoting the location of the line scan (red line, *x* direction) to quantify the displacement. **b**. Plot of displacement field (deformation) across the selected line (red line) for SASS materials patterned with differing numbers of tiles. The blue, green, and red plots denote SASS films with 1 x 1, 5 x 5, and 9 x 9 arrays, respectively. **c.** First derivative of displacement field (strain tensor) from plot in **b**, which shows the strain capacitance of the interstitial spaces between the responsive squares. Note that in this model, we fixed the center of the bottom of the supporting layer. This is why the plot shown in **b** had negative values. In other words, the whole material deforms toward the center, where a positive value represents a deformation toward the positive x-axis direction, and negative values indicate deformation in the opposite direction.

Materials and Methods

Materials. Sodium pyrophosphate decahydrate ($Na_4P_2O_7 \cdot 10H_2O$, ≥99%), anhydrous ferric chloride ($FeCl_3$, ≥97%), ethylene glycol (EG, ≥99%), sodium acetate (NaAc, ≥99%), sodium hydroxide (NaOH, ≥99%), tetraethoxysilane (TEOS, ≥99%), ammonium hydroxide ($NH_3 \cdot H_2O$, 25%~28%), Poly(4-styrenesulfonic acid-co-maleic acid) sodium salt (PSSMA, Mw~20k, SS:MA=1:1), D-isoascorbic acid (D-iAA,), N-isopropylacrylamide (NIPAM, ≥99%), 2,2-dimethoxy-2-phenylacetophenone (Irgacure, ≥99%), poly(ethylene glycol) diacrylate (PEGDA, Mn~700), and (-)-riboflavin (≥98%) were purchased from Sigma-Aldrich (St. Louis, MO). Laponite XLG was generously provided by BYK Additive Inc. (Louisville, KY). Anhydrous ethanol was purchased from Decon Labs Inc. (King of Prussia, PA). Amine terminated tetra-polyethylene oxide (4arm-PEG-NH_2, Mw~10k) was purchased from Laysan Bio Inc. (Arab, AL). Pentaerythritol tetra(succinimidyloxyglutaryl) polyoxyethylene (tetra-PEG-NHS, Mw~10k) was purchased from NOF America Corporation (White Plains, NY). Sylgard® 184 and its curing agent were purchased from Dow Corning Corporation (Midland, MI). Deionized (DI) water was purified using a Barnstead Nanopure water system (18.2 MΩ resistivity). Delrin® (Polyoxymethylene Resin) sheets were obtained from McMaster-Carr (Douglasville, GA).

Fabrication of SASS. An overview of the process for preparing SASS films is illustrated in **Figure 1f**, and is comprised of several steps that are detailed below. Briefly, the first step involves the synthesis of magnetic nanoparticles (step A). These are then aligned and crosslinked within a Delrin® mold (step B) to create a patterned responsive photonic crystal film (step C). The responsive photonic crystal was subsequently cut using a patterned Delrin® grid. Next, the supporting polymer film was poured over the responsive photonic crystal array. Finally, the structure was allowed to cure to generate the SASS film (step D).

A. Synthesis of $Fe_3O_4@SiO_2$ core-shell nanoparticles (MNPs). $Fe_3O_4@SiO_2$ core-shell nanoparticles were synthesized according to previously developed methods.[6] Briefly, for particles with an average diameter of 180 nm, 0.65 g $FeCl_3$, 40 mL EG, 3.0 g NaAc, 1.05 g PSSMA, 14 mg D-iAA, and 120 μL DI H_2O were added consecutively into a parafilm sealed beaker. After vigorous magnetic stirring for about 40 min, a homogeneous mixture formed and then 0.6 g NaOH was added. The mixture was stirred for 1-2 h until all the NaOH was completely dissolved. The mixture was then transferred into a capped 50 mL Erlenmeyer flask and then allowed to react in a preheated oven (190 °C) for 9 h. The Fe_3O_4 products were separated from the solution using an external rare-earth (neodymium-iron-boron) magnet and washed. Initially, the particles were washed with 30 mL of 50 v/v% ethanol three times, and then washed three additional times with DI water.

After the washing steps described above, the magnetite particles were re-dispersed in 30 mL of DI water. A 12 mL aliquot of this dispersion was then mixed with 80 mL ethanol and 4 mL ammonium hydroxide (25-28 wt%) under vigorous mechanical stirring for 1

min. This solution was warmed by using a water bath at 50 °C. Subsequently, two aliquots of 0.4 mL TEOS were added every 20 min. Finally, the reaction products were washed with ethanol three times by using magnetic separation for each wash.

To generate particles with an average size of 210 nm, we followed the steps described above with two exceptions. First, the amount of H_2O used was decreased to 105 μL. Second, the TEOS was added in three aliquots (rather than two): 0.4, 0.4, and 0.2 mL at 20 min intervals.

B. **Synthesis of pure silica nanoparticles.** Silica nanoparticles (~300 nm) were synthesized by the well-established stober method.[7] 50 mL ammonium solution was made by mixing 9 mL ammonium hydroxide (25-28 wt%), 16mL ethanol, and 25 mL D.I. H_2O. This solution was swiftly added to 50mL 0.4 M TEOS ethanol solution under vigorous stirring. After reacting for 2h, the particles were centrifuged and washed three times with ethanol to collect monodisperse silica nanoparticles. TEM indicated that the average particle size was approximately 300 nm.

C. **Fabrication of Delrin® mold and gel cutting tools**. Square shaped sheets of Delrin® with a thickness of 0.125 inch (0.3175 cm) were cut into the desired shapes using a laser cutter (Universal Laser Systems VLS 4.60, featuring a 60-watt CO_2 laser). The patterns were designed using the AutoCAD software package.

D. **Synthesis of responsive photonic film.** The as-obtained $Fe_3O_4@SiO_2$ particles from the protocol (described above) were redispersed in 12 mL of ethanol, and then 3 mL of this solution of $Fe_3O_4@SiO_2$ was redispersed in EG solution containing 8 mg riboflavin, followed by adding 0.09 g Irgacure, 225 μL PEGDA, and 0.45 g NIPAM. The mixture was vortexed for 10 s to obtain a homogeneous solution that was then sonicated for 5 min in the dark. We describe this mixture as the "precursor solution" in subsequent steps. A 3 cm × 3 cm Delrin mold covered with a piece of transparent petri dish was used to fabricate the responsive photonic crystal layer. For each synthesis, 350 μL precursor solution was injected into the mold and exposed to a magnetic field of approximately 245 Gauss (determined using a WT10A teslameter). Finally, the precursor solution was cured with a 100 W high intensity UV lamp (365 nm, Analytik Jena US company) for 10 min. The as-obtained thin film was washed with DMF and H_2O three times, respectively, then was stored in water for further use. Notably, for special shapes (fish and leaf), the Delrin® molds were deliberately fabricated into the required shapes by using a laser cutter as described above using AutoCAD to draw the design.

E. **Patterning of SASS.** The as-synthesized responsive photonic film was first cut by firmly pressing a patterned Delrin® grid (**Figure S5**, fabricated by a laser cutter, as noted above). This was performed on a clean petri dish surface. Prior to the preparation of the PEG supporting layer, two precursor solutions were prepared. The first (precursor A) was prepared using 750 μL deionized water and 0.03 g Laponite XLG

that were mixed together in a 2 mL vial using a magnetic stir bar until the solution became clear. To this Laponite XLG solution, 750 μL of 0.1 M $Na_4P_2O_7/H_3PO_4$ buffer (pH=7.2) and 0.12 g tetra-PEG-NH$_2$ were added and completely dissolved through vigorous stirring and sonication. The second precursor solution (B) was prepared using 0.12 g tetra-PEG-NHS that was dissolved in 600 μL $Na_4P_2O_7/H_3PO_4$ buffer (pH=7.2) under vigorous stirring and sonication. Both precursors A and B were stored in an ice box for 20 min before mixing in order to slow the gelation rate. After cooling precursors A and B, the solutions were mixed together for 10 s using a magnetic stir bar, then quickly poured into a specific Delrin® mold (**Figure S5**) and sandwiched with the grid-cut photonic film that was placed on a petri dish. The gelation process was complete within 15 min at room temperature.

Figure S5. Photographs of Delrin® mold (left) and Delrin® gel cutting grids (right) used in this paper.

Characterization. TEM images were acquired with an Hitachi HT-7700 with 80 kV accelerating voltage. SEM images were obtained using a Topcon DS-130F Field Emission SEM. Digital photographs and videos were recorded with an iPhone 6s. Dynamic surface temperature change was monitored by an Etekcity Lasergrip 1080 Non-Contact Digital Laser Infrared Thermometer Temperature Gun (instrument temperature range is -50 °C to 550 °C). Dynamic light scattering (DLS) was performed with a NanoPlus Zeta / Nano Particle Analyzer at 25 °C. UV light intensity was determined by AMTAST UVA365 UV light meter. Gel deswelling ratio was measured by a digital caliper. White LED illumination was performed using a Cygolite Metro 800 with light intensity of 800 lumen (distance to the sample: 3 cm).

Solar responses were tested with natural sunlight during the daytime between the hours of 1 pm to 3 pm during the months of June and July (location: 33°47'29.6"N 84°19'36.3"W). All experiments were conducted indoors at constant temperature of approximately 23 °C with air conditioning. Note that the sunlight passed through a glass window and a PDMS film before reaching the SASS samples. Accordingly, the actual sunlight power density may be up to 20% lower than the outdoor solar density due to the absorption of PDMS and glass, and the interfacial reflection.

Laser response test were conducted with a 50-80 mW 532 nm Green Laser Module with

TTL and Fan (12V) purchased from OdicForce Lasers (Surbiton, UK). The equipment set is described in **Figure 5a**. Note that the SASS sample was totally immersed in water while the laser stimulation experiments were conducted.

Reflectivity spectra were measured with a FLAME-S-VIS-NIR Spectrometer equipped with a premium 400 μm reflection probe (Ocean Optics Inc., Dunedin, FL). The spectrometer was calibrated with a diffuse reflectance standard (PTFE) prior to all the measurements. All the spectra data were recorded through the OceanView 1.6.3 software package.

Uniaxial tensile tests were conducted using a TestResources 100Q Universal Testing Machine (Shakopee, MN). Samples were mechanically loaded at a rate of 5 mm/min until failure. A CCD camera was used to capture optical marker motion, while an in-house LabVIEW (National Instruments, Austin, TX, USA) program was used to synchronize marker locations and load information with each video frame. Young's moduli were quantified as the slope of the stress-strain curve.

All optical imaging was performed using a Nikon Eclipse *Ti* microscope, operated with Nikon Elements software, a 1.49 NA CFI Apo 100x objective, perfect focus system, LED light source along with a laser launch excitation source. An RICM filter cube with a 535 nm excitation filter was employed to visualize the particle chains. To image the polymer autofluorescence we used a quad filter cube set (Chroma TRF89902-EM - ET - 405/488/561/647 nm) while exciting the sample using a TIRF 405 nm excitation launch with 80 mW power. ImageJ was used to analyze the intensity change of the time lapse video.
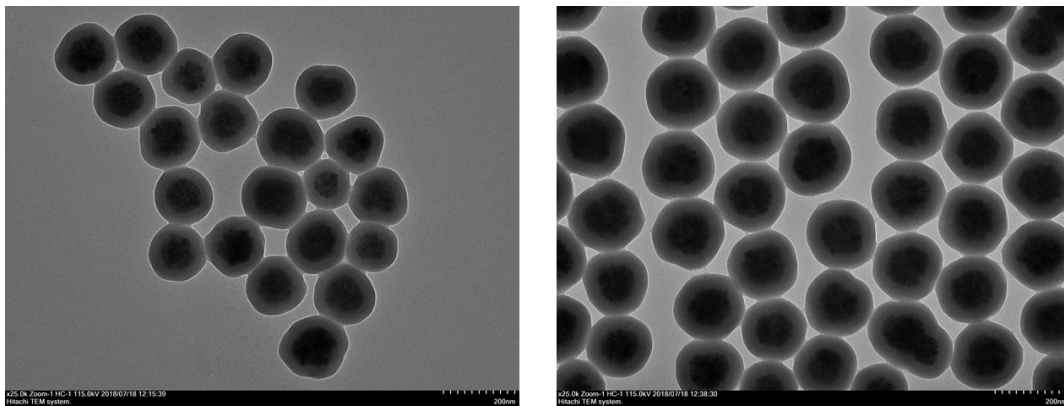
Figure S6. TEM images of 180 nm (left) and 210 nm (right) $Fe_3O_4@SiO_2$ nanoparticles. The diameters were determined by calculating the average diameter of over 100 particles in TEM images (scale bar 200 nm).
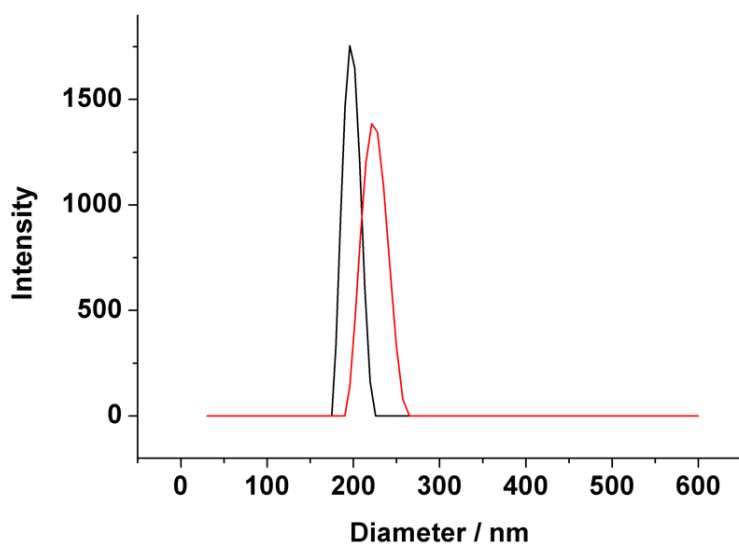
Figure S7. Representative dynamic light scattering (DLS) spectra of two different sizes of particles. The average hydrodynamic diameter of the smaller particles was 196 ± 3.1 nm which is consistent with the TEM determine size of 180 nm. The large particles displayed diameter of 223 ± 4.7 nm and is consistent with the 210 nm diameter determined from TEM. Note that DLS results on average size of particles is greater than the TEM measurement due to the solvent layer surrounding the particles. The reported DLS diameters were averaged from five measurements.
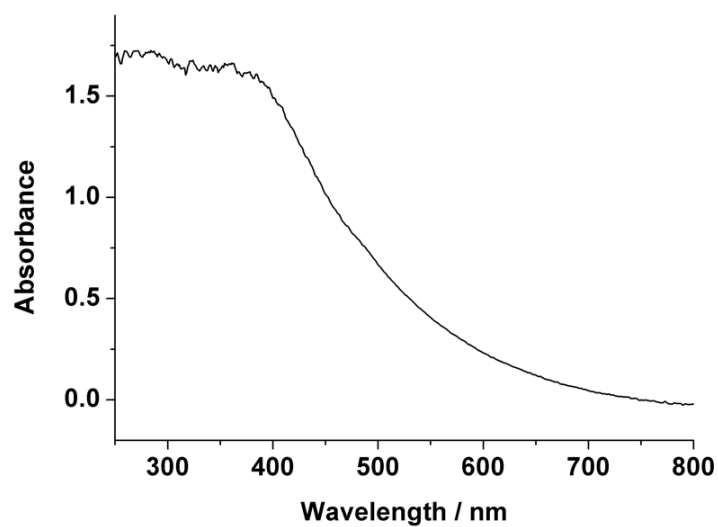
Figure S8. A UV-vis absorbance spectrum of a diluted $Fe_3O_4@SiO_2$ dispersion (~0.001 wt%). The particles have strong absorbance in the UV region that drops down in the visible, in agreement with previous reports.[1]

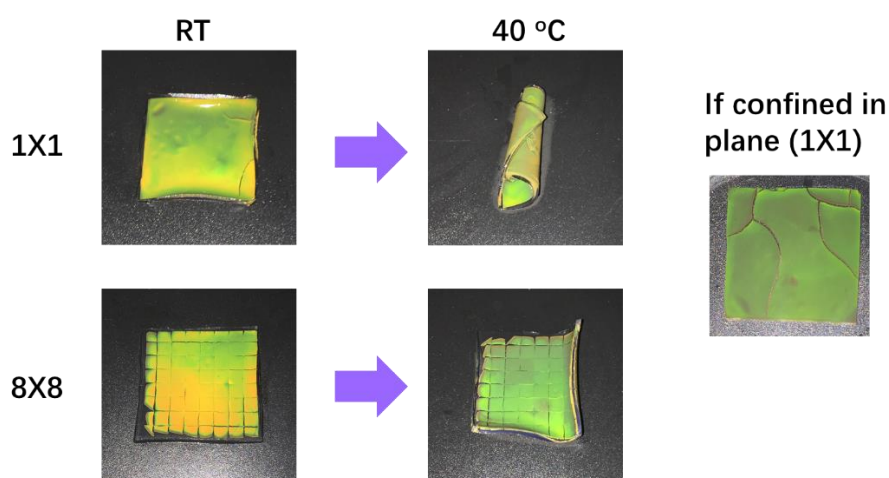# Supplementary S3: Deformation of SASS materials

Figure S9. Photographs comparing deformation of SASS 1 x 1 and 8 x 8 films. The films were about 3.4 x 3.4 cm at room temperature. The samples were heated by using a water bath and were removed from the water in order to acquire the photographs.

As further evidence supporting the importance of the segmented structure for reducing the deformation of SASS materials, we also include photographs depicting the deformation of free-standing SASS films with differing segmentation patterns (**Figure S9**). Unlike the results presented in **Figure 2e** and **f** in the main text, these SASS materials were allowed to bend freely without any restriction. Based on the images, the deformation of 1 x 1 segmentation is more significant compared to that of the 8×8 segmented SASS, validating the experimental results presented in **Figure 1d**. Interestingly, due to the low mechanical strength of pNIPAM responsive PC gels, the 1 x 1 segmented SASS cracks and breaks apart because it was sandwiched and forced to remain in a 2D plane (photograph to the right of **Figure S9**). The deformation predicted by COMSOL in the main text (**Figure 1d**) was not observed in these experiments because modeling assumed that both layers are unbreakable. Nevertheless, we found that the 8 x 8 segmented structure is less likely to crack due to the diminished deformation and low average forces on the plane (as shown in **Figure S4**).
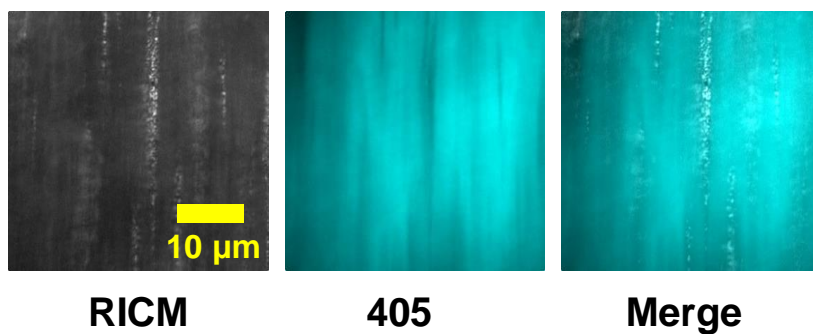
RICM   **405**   **Merge**

Figure S10. Microscopy images of **a** cross-section of responsive layer of SASS observed by different channels and their merged image. Note that the patterns observed by RICM and the 405 nm channels are highly co-localized.
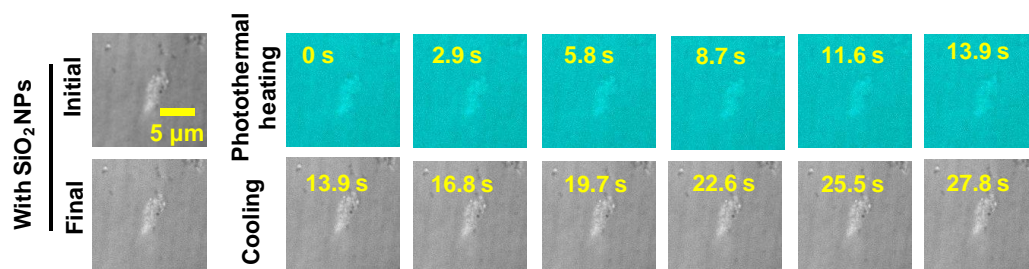
Figure S11. A control experiment of photothermal heating in a SASS sample which the MNPs were replaced with pure silica nanoparticles (d=300 nm) in the responsive layer. Time lapse images in both photothermal heating and cooling process show no obvious change on particle patterns, which indicates magnetite plays an important role on photo-thermal heating of SASS material.

Supplementary S4: Calculation of photo-thermal efficiency of MNPs

The photo thermal efficiency was calculated by the equation set below

$$\sum_i C_i m_i \,{dT}/{dt} = P_{ab} - P_{pass} \qquad\qquad \text{(equation S9)}$$

$$\eta = {P_{ab}}/{P_{in}} \qquad\qquad \text{(equation S10)}$$

Where C_i stands for the heat capacitance of each component inside the cuvette system. mi stands for the mass of each component inside the cuvette system. P_{ab} stands for the power that absorbed by the sample. P_{pass} stands for the power of light that pass through the sample (not being absorbed). dT/dt is the rate of sample heating. P_{in} stands for the power input of light which can be calibrated by a UV light meter. η is the photo thermal efficiency.

Because nearly 100% of MNPs dispersion consists of water and almost all the light passing through the sample is absorbed ($P_{pass} \approx 0$). Equation 9 can be further simplified as

$$C_w m_w \,{dT}/{dt} = P_{ab} \qquad\qquad \text{(equation S11)}$$

Where C_w and m_w are the heat capacity of water and the mass of water respectively.

dT/dt can be measured through the slope of the tangential line (red dash line) in Figure 3e (dT/dt=0.01013 K/s). Also, according to UV light meter, P_{in}=76.83 mW; C_w and m_w are known for 4.19 J/(g·K) and 1.5 g. As a result, η=4.19*1.5*0.01013*1000/76.83≈81.8%.
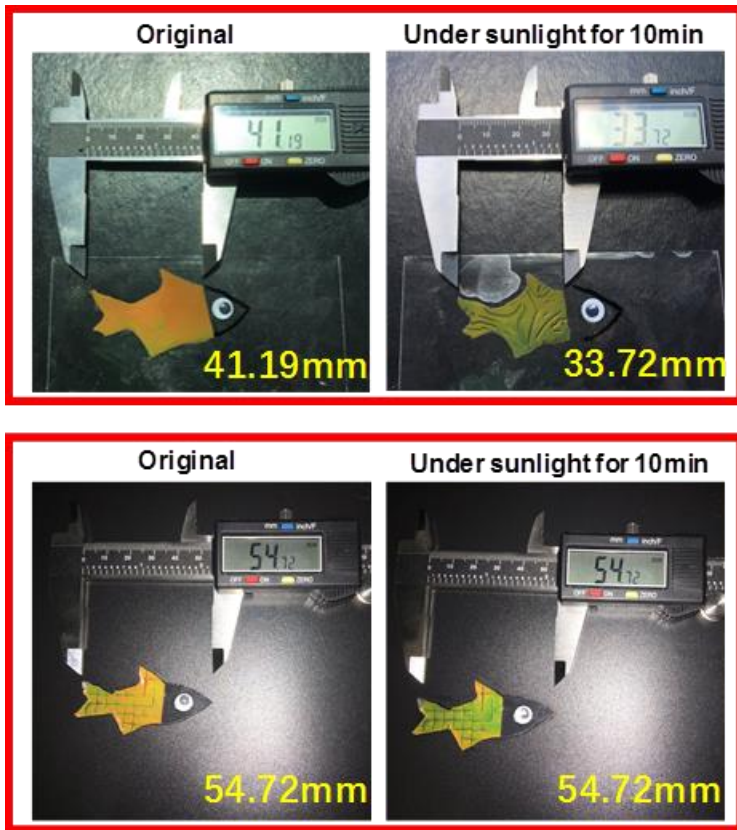
Figure S12. Photographs of fish-shaped RPC and SASS materials before and after exposure to natural sunlight for 10 minutes. The caliper reading is displayed in yellow for clarity and demonstrates the advantage of the SASS design (upper images of traditional responsive PC, and lower images of SASS).

Supplementary Movie captions:

Movie S1. Time-lapse video of aligned MNPs (d=180 nm) in the responsive layer collected during irradiation with a 405 nm laser. The video was collected with a 100x oil immersion objective in the 405 nm channel and has 70 frames in total with 4.83 fps. Observed changes in the nanochain pattern are due to photothermal heating since the observation plane is constant. (displayed with x7 speed)

Movie S2. Time-lapse video of aligned MNPs (d=180 nm) in the responsive layer collected during sample cooling after the 405 nm laser irradiation was stopped. The video was collected with a 100x oil immersion objective in the RICM channel and has 70 frames in total with 4.83 fps. Observed changes in the nanochain pattern are due to gel recovery after photo-thermal heating since the observation plane is constant. (displayed with x7 speed)

Movie S3. Time-lapse video of pure silica nanoparticles (d=300 nm) in the responsive layer collected during irradiation with a 405 nm laser. The video was collected in the 405 nm channel and has 70 frames in total with 4.83 fps. (displayed with x7 speed)

Movie S4. Time-lapse video of pure silica nanoparticles (d=300 nm) in the responsive layer collected after 405 nm laser irradiation. The video was collected in RICM channel and has 70 frames in total with 4.83 fps. (displayed with x7 speed)

Movie S5. A typical SASS sample when irradiated with a 532 nm laser. One square of the array was irradiated for 2 s followed by 11 s of cooling down. Upon irradiation with the laser the observed color changes from green to blue due to photothermal heating. After cooling the square returns to its original state. Only the square exposed to the laser light exhibits a color change. Note that the size of each square is 4 mm x 4 mm.

References

1. Tang, J.; Myers, M.; Bosnick, K. A.; Brus, L. E., Magnetite Fe3O4 Nanocrystals: Spectroscopic Observation of Aqueous Oxidation Kinetics. *J. Phys. Chem. B* **2003,** *107*, 7501-7506.

2. Weissman, J. M.; Sunkara, H. B.; Albert, S. T.; Asher, S. A., Thermally Switchable Periodicities and Diffraction from Mesoscopically Ordered Materials. *Science* **1996,** *274*, 959-963.

3. Aguirre, C. I.; Reguera, E.; Stein, A., Tunable Colors in Opals and Inverse Opal Photonic Crystals. *Adv. Funct. Mater.* **2010,** *20*, 2565-2578.

4. Philipp, M.; Aleksandrova, R.; Müller, U.; Ostermeyer, M.; Sanctuary, R.; Müller-Buschbaum, P.; Krüger, J. K., Molecular versus Macroscopic Perspective on the Demixing Transition of Aqueous PNIPAM Solutions by Studying the Dual Character of the Refractive Index. *Soft Matter* **2014,** *10*, 7297-7305.

5. Sadd, M. H., *Elasticity: theory, applications, and numerics*. Academic Press: Oxford. 2009; pp 31-53

6. Dong, Y.; Wen, B.; Chen, Y.; Cao, P.; Zhang, C., Autoclave-Free Facile Approach to the Synthesis of Highly Tunable Nanocrystal Clusters for Magnetic Responsive Photonic Crystals. *RSC Adv.* **2016,** *6*, 64434-64440.

7. Stöber, W.; Fink, A.; Bohn, E., Controlled Growth of Monodisperse Silica Spheres in the Micron Size Range. *J. Colloid Interface Sci.* **1968,** *26*, 62-69.